Quantum-Based Modulated Microwave Waveforms

Akim A. Babenko, *Graduate Student Member, IEEE*, Nathan E. Flowers-Jacobs, *Member, IEEE*, Anna E. Fox, *Senior Member, IEEE*, Paul D. Dresselhaus, Zoya Popović, *Fellow, IEEE*, and Samuel P. Benz, *Fellow, IEEE*

***Abstract*—This article presents a superconducting voltage source that generates modulated microwave waveforms with quantum-based stability. The voltage source—an RF Josephson Arbitrary Waveform Synthesizer (RF-JAWS)—uses a superconducting IC with an array of 4500 series-connected Josephson junctions (JJs) that are embedded in a coplanar waveguide (CPW) transmission line. The JJs are driven with 100-ps wide current pulses that force each JJ to generate voltage pulses with a quantized integrated area. A pulse sequence is created using a delta–sigma (Δ–Σ) algorithm to generate a 101-tone waveform with a 40-MHz instantaneous bandwidth around 1005 MHz with a flat power distribution of −53 dBm and a Schroeder phase distribution. The JJ's quantum-based nonlinearity produces an amplitude stability with respect to various drive and bias parameters of ±0.005 dB and a detrended phase stability of ±0.05°. The stability of the source is verified without the need for calibrated measurements. Another Δ–Σ pulse sequence generates a 10-MHz quadrature-phase shift-keying (QPSK) waveform on a 1005-MHz carrier that has the same stability and the mean error vector magnitude (EVM) of −48 dB. This work is a step toward creating a quantum-based reference source for power and cross-frequency phase calibrations, as well as a reference-modulated signal source for calibrating telecommunication links.**

***Index Terms*—Error vector magnitude (EVM), Josephson junctions (JJs), pulse measurements, superconducting integrated circuits, superconducting microwave devices.**

I. Introduction

REFERENCE multitone waveforms are essential for component- and system-level testing in modern RF communications [1]. For example, reference comb generators are used for microwave waveform measurements [2]. These comb generators provide a stable, periodic pulsed waveform that serves as a harmonic phase reference (HPR) for calibrating frequency-sweeping measurement receivers [3]. In this article, a Josephson-junction array is demonstrated as a quantum-based RF signal source for multitone and quadrature-phase shift-keying (QPSK) modulated waveforms, with its simplified operation scheme shown in Fig. 1.

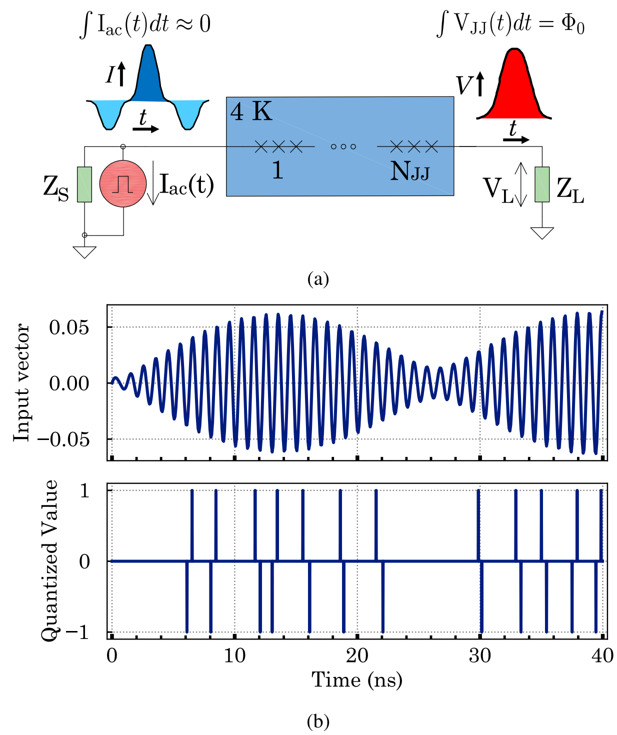

Fig. 1. (a) Simplified circuit diagram of an RF-JAWS. Drive current pulses I_{ac} produce a voltage V_{JJ} across an array of N_{JJ} JJs (crosses) monolithically integrated in series in a matched transmission line. Each nonlinear JJ element creates precise voltage pulses when driven by current pulses with a range of pulse shapes. (b) Calculated encoding of an arbitrary waveform (101-tone input, top) using a delta–sigma (Δ–Σ) pulse-density modulation algorithm (quantized JJ pulses, bottom). The JJ output spectrum is calculable based on the known constant integrated voltage (total magnetic flux) per pulse equal exactly to the magnetic flux quantum Φ_0.

The desired characteristics of comb generators are: 1) high frequency of the power spectral density (PSD) roll-off for sufficient SNR over a wide frequency range, translating to fast pulse edges and 2) narrow frequency spacing for high sweep resolution, translating to a low pulse-repetition frequency. The bandwidth of typical frequency combs used for instrumentation is on the order of 70 GHz at a 10-MHz repetition frequency [4], [5], with the PSD rolling off to about −90 dBm at the highest frequency with −60 dBm at 10 MHz.

The phase spectrum of the frequency combs can be of any type (uniform, pseudorandom, Schroeder, etc.) and is calibrated using electrooptic sampling (EOS) [6]. Due to the

Manuscript received 21 April 2023; accepted 10 June 2023. The work of Akim A. Babenko was supported by the National Institute of Standards and Technology (NIST) under the NIST-PREP Fellowship. *(Corresponding author: Akim A. Babenko.)*

Akim A. Babenko was with the Department of Electrical, Computer and Energy Engineering, University of Colorado, Boulder, CO 80309 USA. He is now with the Jet Propulsion Laboratory, Pasadena, CA 91109 USA (e-mail: akim.a.babenko@jpl.nasa.gov; akim.babenko@colorado.edu).

Nathan E. Flowers-Jacobs, Anna E. Fox, Paul D. Dresselhaus, and Samuel P. Benz are with the Superconductive Electronics Group, National Institute of Standards and Technology (NIST), Boulder, CO 80305 USA (e-mail: nathan.flowers-jacobs@nist.gov; anna.fox@nist.gov; paul.dresselhaus@nist.gov; samuel.benz@nist.gov).

Zoya Popović is with the Department of Electrical, Computer and Energy Engineering, University of Colorado, Boulder, CO 80309 USA (e-mail: zoya.popovic@colorado.edu).

Color versions of one or more figures in this article are available at https://doi.org/10.1109/TMTT.2023.3297364.

Digital Object Identifier 10.1109/TMTT.2023.3297364

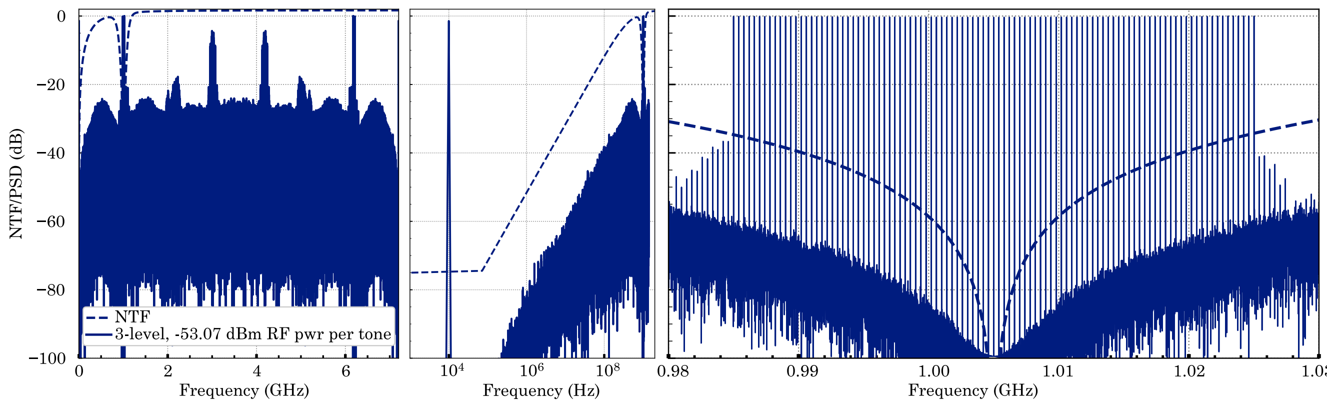

Fig. 2. Calculated RF-JAWS waveform spectrum (solid line) and the NTF (dashed line) used in the three-level Δ–Σ algorithm to create the waveform. The full bandwidth of the digital pattern $w[n]$ is shown on the left; the middle plot highlights the 10-kHz tone and the right plot shows the 101-tone with flat PSD at an average -53.07 dBm across 50 Ω within a 40-MHz bandwidth around 1005 MHz and with Schroeder phase distribution. The spectrum is normalized to the peak PSD.

fixed 200-MHz pulse-repetition frequency of the EOS [7], comb generators have limited flexibility on the frequency grid that is most often at 10 MHz. The use of calibrated arbitrary waveform generators (AWGs) is shown to provide arbitrary frequency grids and therefore more versatile multitone waveforms over a 100-MHz frequency range [8]. There is also a demonstration of a millimeter-wave comb generator utilizing upconversion with an instantaneous bandwidth over 2 GHz [9]. The power-per-tone of the AWG-generated multitone is typically on the order of -60 dBm for the typical 10-MHz frequency grids.

For nonlinear characterization, arbitrary multitone periodic signals are used [10], [11], [12]. These signals are typically generated using AWGs to cover a wide range of modulation types, corresponding to different spectral masks, signal statistics, and peak-to-average power ratios (PAPRs) [1]. Traceable modulated signal sources at millimeter waves that utilize upconversion were also demonstrated for connectorized [13] and over-the-air (OTA) testing [14], [15]. The bandwidths of the modulated signal sources also range from tens of megahertz to a few gigahertz at the expense of the number of tones and power per tone.

We are developing the RF Josephson Arbitrary Waveform Synthesizer (RF-JAWS) as a quantum-based reference source of arbitrary microwave waveforms. The RF-JAWS circuit consists of an array of thousands of Josephson junctions [JJs; Fig. 1(a)] operating at cryogenic temperatures (4 K in this work). The JJs are embedded in a superconducting transmission line and are driven by a pattern of current pulses. A single pulse is shown in Fig. 1(a) and a pulse pattern in Fig. 1(b) [16], [17], [18], [19]. Within a range of drive, bias, and environmental parameters, each drive current pulse forces each JJ in the array to produce a single voltage pulse with a dc component exactly equal to a single magnetic flux quantum $\Phi_0 = h/2e$, where h is the Planck constant and e is the elementary charge. This direct quantum-based connection to defined fundamental constants enables dc Josephson voltage standards with accuracies better than 1 nV/V [20]. The long-term goal of RF-JAWS development is to extend quantum-based sources to GHz frequencies, as well as to complement and eventually replace the current reference microwave-modulated signal sources.

This article first briefly introduces RF-JAWS in Section II. Section III demonstrates the correct quantum-based operation of an RF-JAWS generating a multitone waveform with improved bandwidth, number of tones, and power per tone compared to state-of-the-art results reported in [21] and [22]. We also demonstrate a QPSK-modulated RF-JAWS waveform in Section IV. This builds on previous work on RF-JAWS signals [21] that showed a four-tone multitone with a limited bandwidth (100 kHz) and power per tone (-57 dBm) and did not validate the system operation. Here, we extend the multitone bandwidth to 40 MHz, number of tones to 101, and power per tone to an average of -53 dBm by improving the drive-current pulse shape with a pulse equalization technique [22]. The RF-JAWS operation is validated by measuring the dc-bias current and pulse-amplitude quantum locking ranges (QLRs), that is, the range of the parameter over which each JJ is correctly generating a single flux pulse for each drive-current pulse.

II. Arbitrary Waveforms Using RF-JAWS

A. Delta–Sigma (Δ–Σ) Modulation

The RF-JAWS system generates calculable, quantum-based arbitrary waveforms by using a Δ–Σ algorithm to determine the sequence of the JJ-generated voltage pulses. A JJ is a circuit element that generates a voltage pulse with an integrated area equal to exactly one magnetic flux quantum Φ_0 when it is driven by a current pulse (Fig. 1(a), [23]) under a range of environmental and operational conditions. When operating in this range, a sequence of three-level drive-current pulses causes every JJ in the array to generate voltage pulses $w[n]$, for the results in this article with a clock rate of 14.4 Giga-pulses per second. At each clock step n, every JJ either generates a positive pulse $w[n] = +1$, a negative pulse $w[n] = -1$, or no pulse $w[n] = 0$. The synthesized output voltage waveform created by these pulses is a convolution of the Δ–Σ pulse pattern with the shape of each JJ voltage pulse $P(t)$ normalized so that $\int_{-\infty}^{\infty} P(t)\, dt = 1$

$$V_{\mathrm{JJ}} = N_{\mathrm{JJ}} \Phi_0 P(t) \otimes \sum_n w[n] \delta(t - n T_{\mathrm{clk}}) \tag{1}$$

where δ is the Kronecker delta function, T_{clk} is the clock cycle period, and N_{JJ} is the number of JJs in the array. The shape of the JJ voltage pulses $P(t)$ depends on the JJ parameters and drive current characteristics and is a source of error in calculating V_{JJ}. However, this error is negligible for the 1-GHz synthesis frequencies, JJ parameters, and drive current pulse shapes used in this article [21], [22], mainly because the JJ voltage pulsewidth is approximately the inverse of the JJ characteristic frequency which for the JJs used in this article is around 18 ≫ 1 GHz.

The Δ–Σ algorithm converts an arbitrary waveform into the train of pulses $w[n]$, which is a natural algorithm for a digital-to-analog converter (DAC) with a high oversampling ratio but only a few (three in this work) discrete amplitude levels. The algorithm's feedback loop has a filter with a noise transfer function (NTF) designed to shape the digitization noise to create an output waveform with a clean spectrum in the bandwidth of interest [24]. A low-pass (LP) NTF is used to encode waveforms from dc to 100 kHz [16], [18], [25], and a bandpass (BP) NTF is used in RF-JAWS systems [19], [21], [22], [26]. The highest synthesis frequencies presented below are limited primarily by the highest available f_{clk} and the feedback parameters of the Δ–Σ modulator [24]. In this article, we chose the synthesis frequencies such that the uncertainties in f_{clk} and other Δ–Σ waveform parameters remain negligible [27].

The spectrum of the pulse sequence $w[n]$ that generates the multitone RF-JAWS waveform is shown in Fig. 2 (solid lines). The sequence is created using a Δ–Σ modulator with a multipole NTF (dashed lines) with stopbands around the frequencies of interest to reduce the background spurs at and around those frequencies [28]. A first-order LP filter for a 10-kHz tone is cascaded with a fourth-order BP filter for the 101-tone signal around 1005 MHz. The RF tones range from 985 to 1025 MHz with a 400-kHz step. This waveform produces an open-circuit V_{JJ} of 0.878 mV rms at 10 kHz and 0.994 mV rms per tone (−53.07 dBm into 50 Ω) around 1005 MHz with an $N_{\text{JJ}} = 4500$ array. The simulated Schroeder phase distribution [29] of the input 101-tone waveform has a 7.151-dB PAPR. The phase of each tone in this Schroeder distribution was calculated as $\left(n^2 \cdot 180/101\right)^{\circ}$, where $n = 1, 2, \ldots, 101$. The total length of the pulse pattern is 500 μs (five periods at 10 kHz) or 7.2 MSa at 14.4 Giga pulses per second.

To further demonstrate the operation of the Δ–Σ modulator, we plot the first 40 ns of the 500 μs long 101-tone waveform in Fig. 1(b). The ideal input waveform for the Δ–Σ algorithm is at the top and the three-level Δ–Σ output $w[n]$ is at the bottom. While the agreement between the input and output is poor over these 40 ns, allowing the algorithm to proceed over a 12 500 times longer period results in a clean spectrum around the frequencies of interest defined by the Δ–Σ NTF (Fig. 2).

B. RF-JAWS System Operation

The diagram of the RF-JAWS system used in this work is shown in Fig. 3. The superconducting IC operates at 4 K and consists of an array of 4500 JJs connected in series in the center conductor of a coplanar waveguide (CPW) transmission line with a nominally 50-Ω characteristic impedance. The details of the superconducting IC design are available in [22] and the fabrication process is described in [30] and [31]. The loading of the CPW line by the 4500 JJs is negligible for $f_t \leq 1$ GHz, given the values for each JJ of $I_c = 9.5$ mA and $R_n = 4$ mΩ used in this work [23].

The drive-current pulses are generated using a 57.6 GSa/s AWG. The pulse pattern $w[n]$ generated by the Δ–Σ algorithm with a clock rate of 14.4 Giga-pulses per second

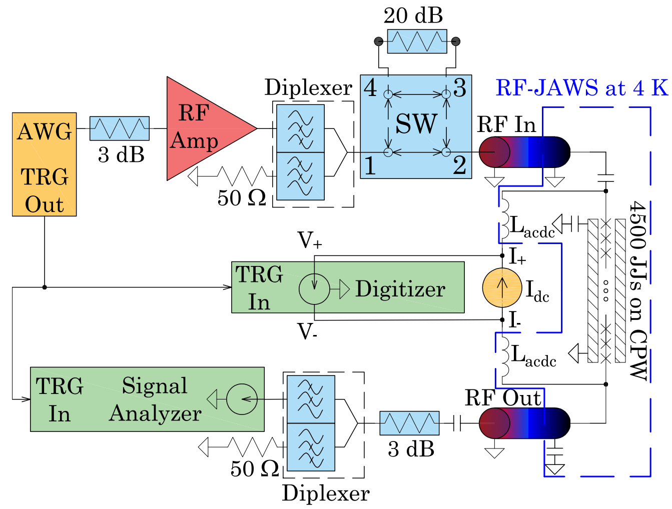

Fig. 3. Block diagram of the RF-JAWS system. The AWG provides the current pulse bias and during normal operation, the switch SW bypasses the 20-dB attenuator (solid SW position; see text for details). The synthesized audio-frequency voltage is measured across the JJ array with the digitizer and the dc current bias is applied using a current source I_{dc}. The synthesized microwave tones are measured with the signal analyzer at room temperature after 3-dB attenuation and LP filtering. The digitizer and the signal analyzer are triggered by the AWG ("TRG Out") for coherent phase measurements.

is nearest-neighbor interpolated to match the AWG sample rate. The analog pulses are then amplified and high-pass filtered by the diplexer and represent the drive-current pulses I_{ac} for the JJ array at 4 K. The peak PSD of the drive-current Δ–Σ pulses I_{ac} is on the order of 20 dBm at the JJ array, compared to around −30 dBm peak PSD of the same Δ–Σ sequence of JJ-generated voltage pulses V_{JJ} [21, Sec. II-A] on the drive-current scale). This necessitates the use of the analog high-pass filtering implemented here with the on-chip diplexers. The diplexer is oriented to create a broadband reflectionless environment for the JJ array. The switch SW is used in the solid position to drive the JJ array through the "RF In" cable. We compensate for the pulse distortion introduced by all of the room-temperature components by using a zero-forcing pulse symmetrization algorithm to digitally filter the programed AWG waveform. See [22] for further details on the instrumentation and zero-forcing algorithm. We use a four-probe configuration to add an additional low-frequency current bias I_{dc} to the JJs and measure the low-frequency voltage V_{JJ} across the JJ array using a digitizer with 22 bits of resolution at 1 MSa/s. Because our modulated signal source operates at zero dc bias, I_{dc} is only used to demonstrate that the system is operating correctly, as will be shown in Section III.

The RF-JAWS output at microwave frequencies is measured at room temperature after being attenuated and LP-filtered to prevent compression of the signal analyzer (see out-of-band high-frequency tones in Fig. 2, left plot). The signal analyzer is used as an in-phase-quadrature (IQ) demodulator to measure complex waveforms [32]. Each microwave waveform measurement involves triggering the signal analyzer at the start of an AWG waveform and taking 400 000 samples of the waveform at 80 MSa/s with the IQ-receiver tuned to 1005 MHz, without averaging. The signal analyzer has a 40-MHz analog bandwidth and the modulated signals used in this article are designed to fit this bandwidth.

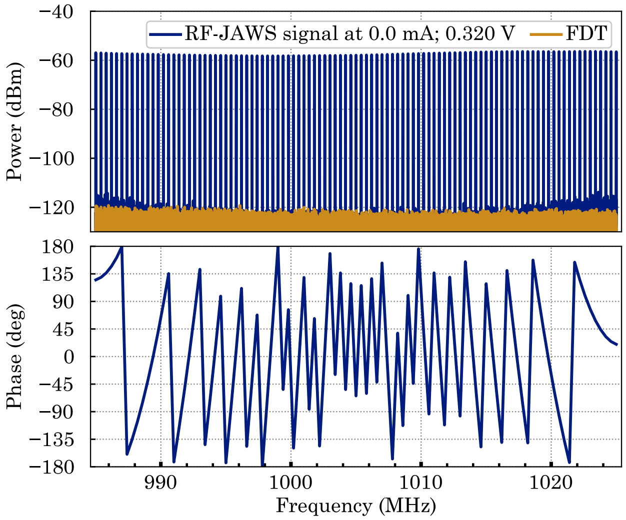

Fig. 4. Measured 101-tone power spectrum generated by RF-JAWS (top, blue tones) and the systematic feedthrough error power spectrum (top, yellow noise). The feedthrough power spectrum is below the measurement noise floor and its phase is therefore not shown.

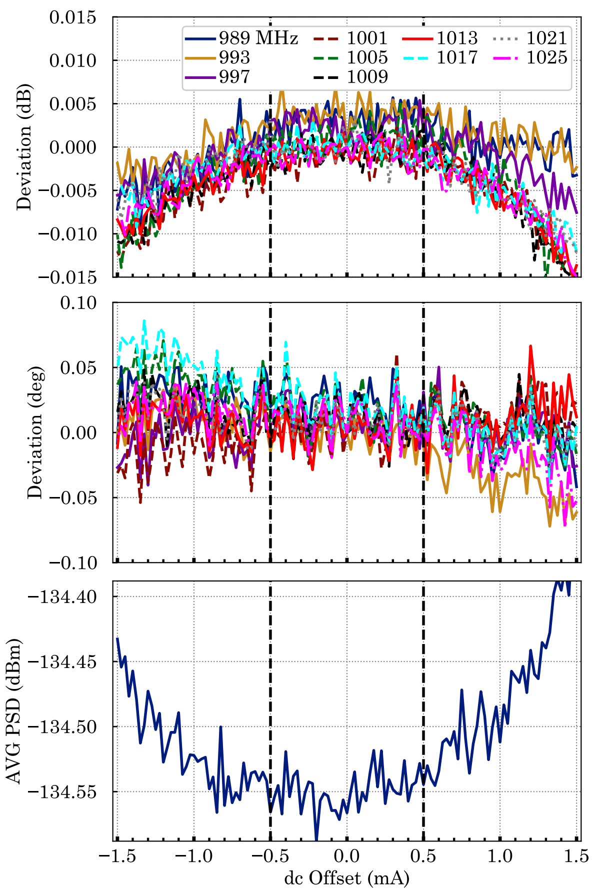

Fig. 5. DC-current offset QLR measurements for the multitone signal generated by RF-JAWS. The shared x-axis is the dc current offset; the y-axes are the change from the 0.0 mA values in: the measured tone power (top); detrended phase (middle) for ten select tones of the multitone; and the average noise PSD between all of the waveform tones (bottom). All of these values are constant within the dc current offset QLR of ± 0.5 mA (vertical dashed lines).

The drive-current frequency components around the measured 1005 MHz can create a systematic error signal at the signal analyzer or another device under test (DUT). As in [22], we measured this error signal by adding a 20-dB attenuator to the drive current using the SW in the state shown by the dashed lines in Fig. 3. This attenuator does not change the input–output signals at the AWG and amplifier, but is large enough that the JJ array responds without pulsing and nearly linearly. The measured spectra at the signal analyzer with the attenuator in place are an upper bound on this systematic error signal.

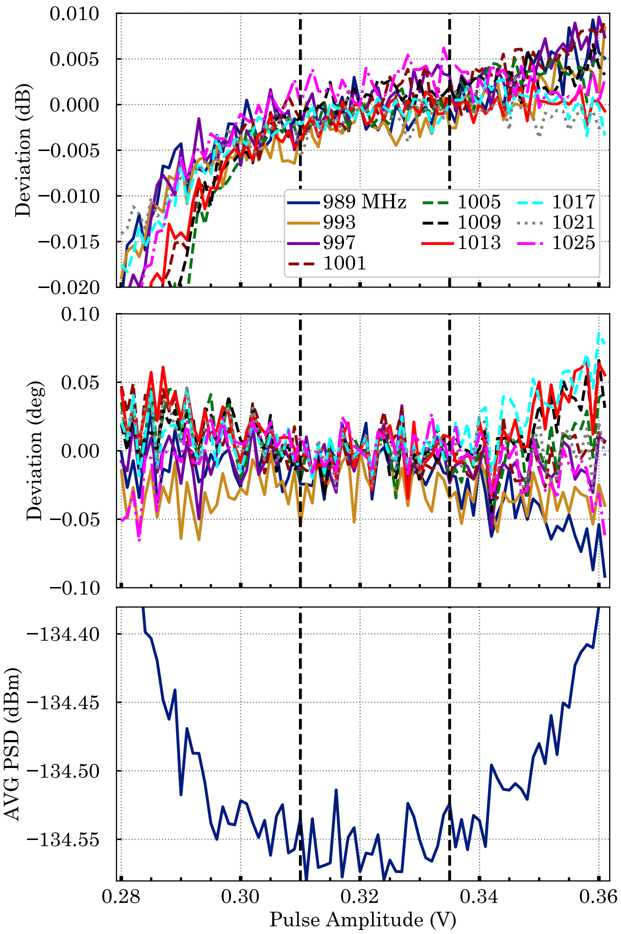

Fig. 6. Pulse-amplitude QLR measurements for the multitone signal generated by RF-JAWS. The shared x-axis is the programed AWG pulse amplitude; the y-axes are the change from the 0.320 $V_{p\text{-}p}$ values in: the measured tone power (top) and detrended phase (middle) for ten tones of the multitone; and the average noise PSD between all of the waveform tones (bottom). All of these values are constant within the AWG pulse amplitude QLR from 0.310 to 0.335 $V_{p\text{-}p}$ (dashed vertical lines).

III. Multitone Synthesis and Measurements

The 101-tone spectrum generated using the RF-JAWS system is shown in Fig. 4. The 101 tones in the measured power spectrum have an average power of −57.35 dBm. In an ideal, lossless 50-Ω RF-JAWS system, we would expect to see an average power of −53.07 based on the calculated 0.994-mV rms open-circuit voltage per tone. The 4.28 loss stems mainly from the 3-dB attenuator, the attenuation inherent in the "RF Out" cabling, and the diplexer (Fig. 3). The impedance mismatch between the networks before and after the JJ array and the frequency response of the signal analyzer also has a small effect. In the future, accurately correcting for these effects will require using a vector network analyzer to move the measurement reference plane to the cryogenic JJ-array as in [26].

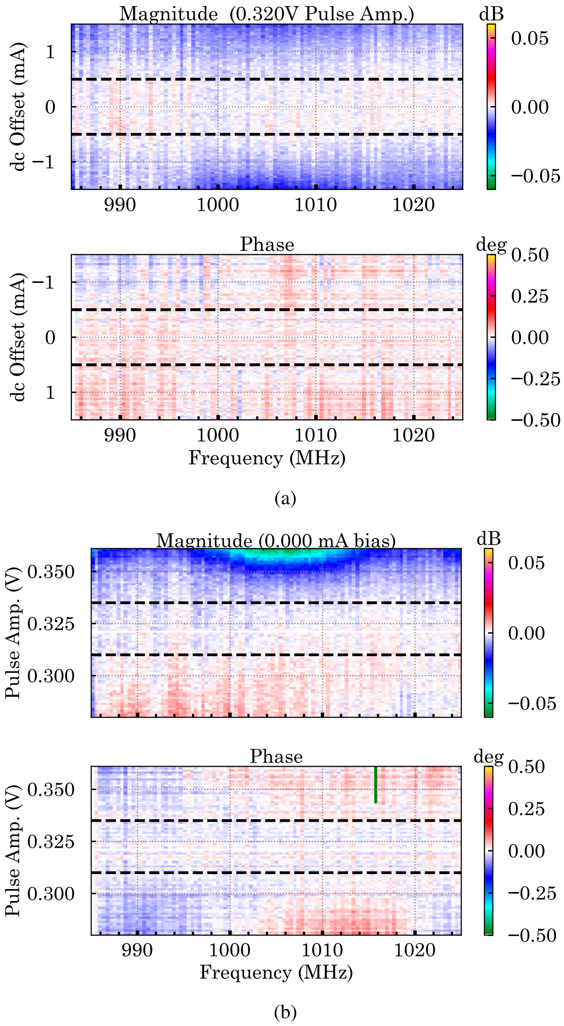

Fig. 7. QLR measurements showing the deviation of each tone amplitude or detrended phase (labeled color bars) from the values at the nominal 0.0 mA I_{dc} and 0.320 $V_{p\text{-}p}$ pulse amplitude for all of the 101 tones (frequency of tone on the x-axes): (a) versus the dc offset current (y-axis) and (b) versus AWG pulse amplitude (y-axis). All of the measured values are constant within each QLR (dashed horizontal lines). See Figs. 5 and 6 for vertical line cuts at ten different tone frequencies.

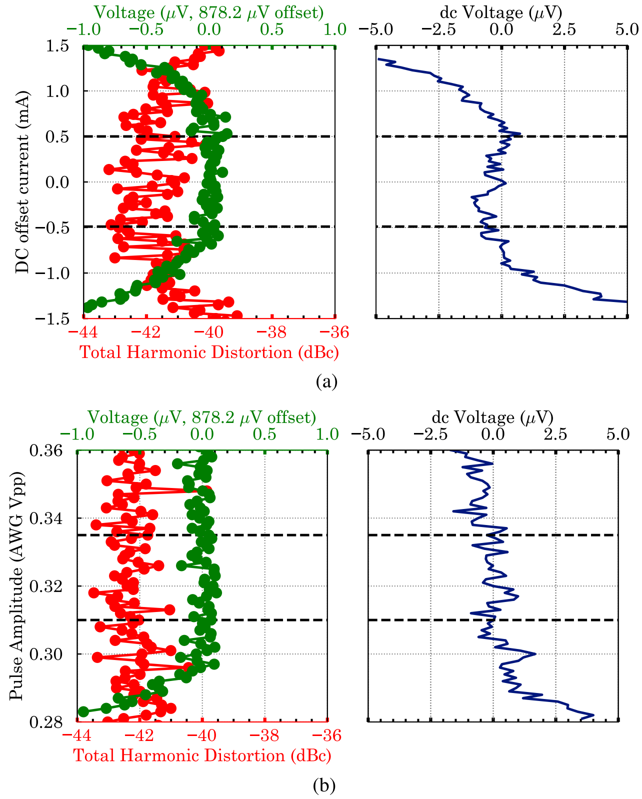

Fig. 8. Low-frequency QLR measurements of the multitone signal generated by RF-JAWS. The shared y-axes are (a) dc offset current and (b) AWG pulse amplitude. Left top axis shows the 10-kHz tone amplitude, left bottom axis is total harmonic distortion, and the right axis is the dc voltage. All of the measured values are constant within parameter QLRs (horizontal dashed lines).

To demonstrate that the RF-JAWS system is generating the 101-tone waveform correctly and each input current pulse is forcing each JJ to create one and only one output voltage pulse (see Section II-A for JJ dynamics review), we measure the QLRs of both the dc current and the AWG pulse amplitude, that is, we measure the range of these parameters over which there is no change in the generated signal, using different ways of quantifying the measured signal. We start with the nominal parameter values used in Fig. 4 of 0.0 mA I_{dc} and 0.320 $V_{p\text{-}p}$ pulse amplitude programed into the AWG.

In Fig. 5, we vary I_{dc} and plot the resulting QLR measurements of the tone magnitudes (top) and detrended phases (middle) at select frequencies in the multitone as well as the background average PSD (bottom) versus applied dc offset. The phase of each tone has a linear dependence on dc current, as expected based on previously published simulations and experiments [27]. We, therefore, linearly detrend the phase using the procedure explained in the Appendix and plot the residual phase variations in the middle plot of Fig. 5. The background average PSD is found by taking the average power over the bandwidth of the 101-tone after removing all of the spectrum points within ±1 kHz of each tone where the PSD is dominated by phase noise [21, Fig. 12]. All of these quantities are constant within the dc offset QLR of ±0.5 mA (vertical dashed lines): the amplitudes of the select tones are constant to within ±0.005 dB; the detrended phases are constant to within ±0.06°; and the average PSD remains at near the signal analyzer noise floor (see Fig. 4).

Similarly, in Fig. 6, we vary the pulse amplitude around the nominal AWG value of 0.320 $V_{p\text{-}p}$ and plot the same measured quantities: selected tone magnitude (top), phase (middle), and background average PSD (bottom). The plot shows a pulse amplitude QLR from 0.310 to 0.335 $V_{p\text{-}p}$ (dashed vertical lines), that is, a 7.8% fractional variation of the programed AWG pulse amplitude over which the measured quantities are similarly constant (±0.005 dB or 0.058% for amplitude and ±0.05° for phase).

In Fig. 7, we plot the same dc bias QLR and pulse amplitude QLR measurements of the tone amplitudes and detrended phases as in Figs. 5 and 6, but use a color plot to show the QLR of each tone. The same QLR ranges and tone variations as in Figs. 5 and 6 (dashed lines) are seen in this visualization of the QLR data.

Within the QLR of a parameter, both the RF and low-frequency spectral components of the generated waveform are independent of the parameter value (up to known sources of error). In Fig. 8, we plot three measured low-frequency spectral metrics over the same ranges of (a) dc offset current and (b) AWG pulse amplitude: the amplitude of the 10-kHz tone (green, left), the total harmonic distortion (red, left), and

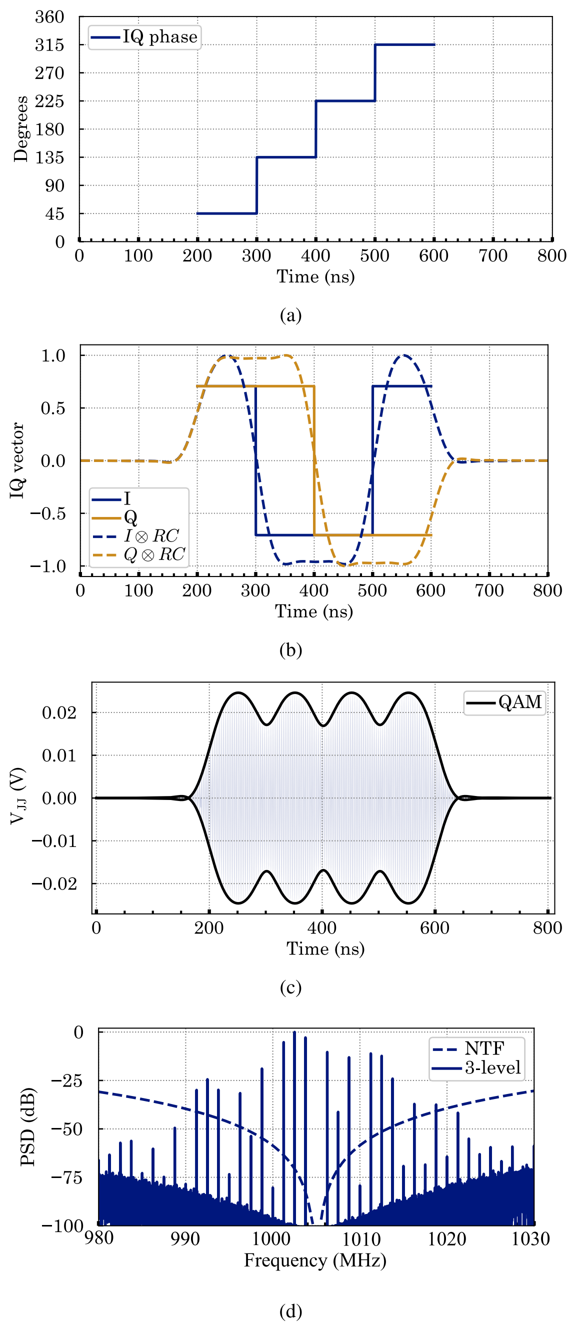

Fig. 9. (a) QPSK phase values. (b) Corresponding ideal (solid) and raised-cosine-filtered (dashed) I and Q components. (c) Calculated QAM JJ voltage waveform on a 1005-MHz carrier. (d) Simulated Δ–Σ (solid) peak-normalized PSDs of the QAM waveform and the corresponding NTF (dashed). $\otimes$ is the convolution operator. RC—raised-cosine.

the dc voltage (blue, right). The QLRs determined from the RF measurements are shown as dashed lines. Over the RF-based QLRs, the low-frequency metrics are also constant: the 10-kHz amplitude deviates from the calculated value of 0.878-mV rms by no more than 100 nV, the THD of −42.5 dBc varies by less than ±1 dB, and the dc voltage changes by less than 1 μV. In general, different QLR metrics will have both different background noise and different sensitivity to patterns of missing or additional voltage pulses. We, therefore, base the QLRs on the metric that results in the smallest (worst) range.

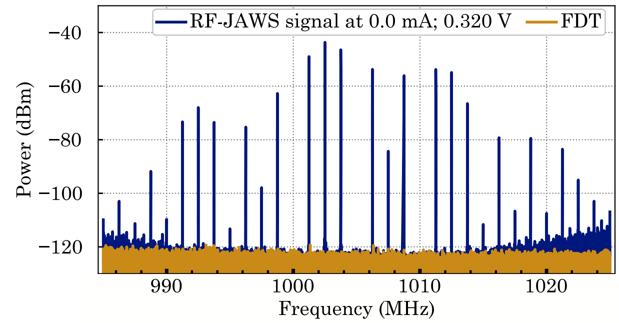

Fig. 10. Measured power spectrum of the 10-MHz QPSK signal on a 1005-MHz carrier generated by RF-JAWS (blue) and the systematic feedthrough error power spectrum (yellow, noise floor).

IV. QPSK Synthesis and Measurements

To further demonstrate the capability of RF-JAWS to generate arbitrary waveforms beyond multitones, we generate a QPSK waveform and show that the system is operating properly by measuring QLRs. The QPSK signal is implemented using a quadrature amplitude modulation (QAM) scheme. This same QAM modulator architecture is typically used to implement other digital BP modulation schemes, for example, QAM-8, QAM-6, and so on [31, Ch. 7].

A. Δ–Σ QPSK Simulations

The process to determine the Δ–Σ sequence $w[n]$ that encodes a QPSK signal is depicted in Fig. 9. The modulation format uses a carrier that has a constant amplitude (envelope) and encodes four symbols in four different phases (45°, 135°, 225°, and 315°, [31, Ch. 7]). We use a symbol clock frequency of 10 MHz based on the signal analyzer analog bandwidth of 40 MHz and generate an ascending-phase, four-symbol sequence, with a no-signal, two-clock-cycles cyclic prefix and same suffix that provide guard intervals [Fig. 9(a)]. We choose this pattern for simplicity, but longer, arbitrary symbol sequences can also be generated with the Δ–Σ algorithm.

Next, the symbols are encoded as in-phase (I) and quadrature (Q) components of the baseband modulation signal [solid lines, Fig. 9(b)]. We then limit the baseband to roughly the signal analyzer's 40-MHz bandwidth by applying a raised-cosine finite-impulse-response (FIR) filter with a roll-off factor equal to 0.9 [see [31, Ch. 6], dashed line in Fig. 9(b)]. Convolution of the baseband samples with the same-length FIR filter results in the end effects that are as long as the original digital waveform. As seen from Fig. 9(b), the baseband samples decay sufficiently within these "guard" intervals.

Finally, we use the I/Q baseband to modulate a 1005-MHz carrier resulting in an 800-ns-long QAM waveform [Fig. 9(c)] with a calculated PAPR of 10.9 dB. This waveform is repeated 625 times (500-ms total length), summed with the same 10-kHz tone used with the multitone waveform, and is input into the same Δ–Σ algorithm as before (see Section II-A) to determine the QPSK pulse sequence $w[n]$. The resulting peak-normalized PSD of $w[n]$ is shown in Fig. 9(d), along with the corresponding NTF. The input waveform and Δ–Σ spectra are nearly identical over the plotted 50-MHz bandwidth and the main tones are separated by 1.25 MHz due to the 800-ns waveform period.

B. Δ–Σ QPSK Measurements

We use the RF-JAWS to generate the QPSK pattern using the same bias/drive settings and digital filtering as for the

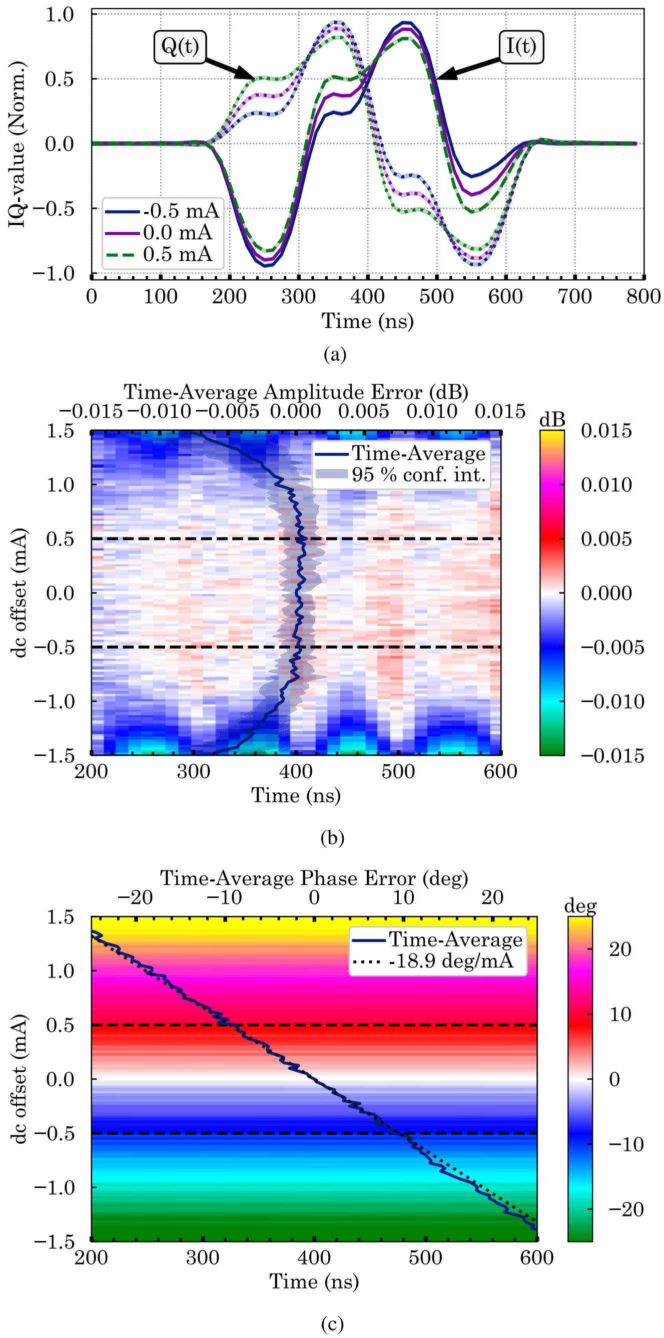

Fig. 11. (a) I and Q components of the QPSK waveforms measured by the signal analyzer at three different dc offset currents. The data are normalized by the peak amplitude of the IQ vector at 0.0-mA dc offset current. (b) Time- and dc-offset-dependent amplitude error shown as a color plot over the time period where the carrier is nonzero. The solid line is the dc-offset-dependent (y-axis) amplitude error (top x-axis) averaged over the plotted time period (95% confidence interval shown as shaded area). (c) Time- and bias-dependent phase errors shown as a color plot. The solid line is the bias-dependent (y-axis) time-average phase error without detrending (top x-axis). A linear fit (dotted line) based on the data within the ±0.5-mA QLR (horizontal lines) is used to detrend the time-average phase error and the result is shown in Fig. 12(a).

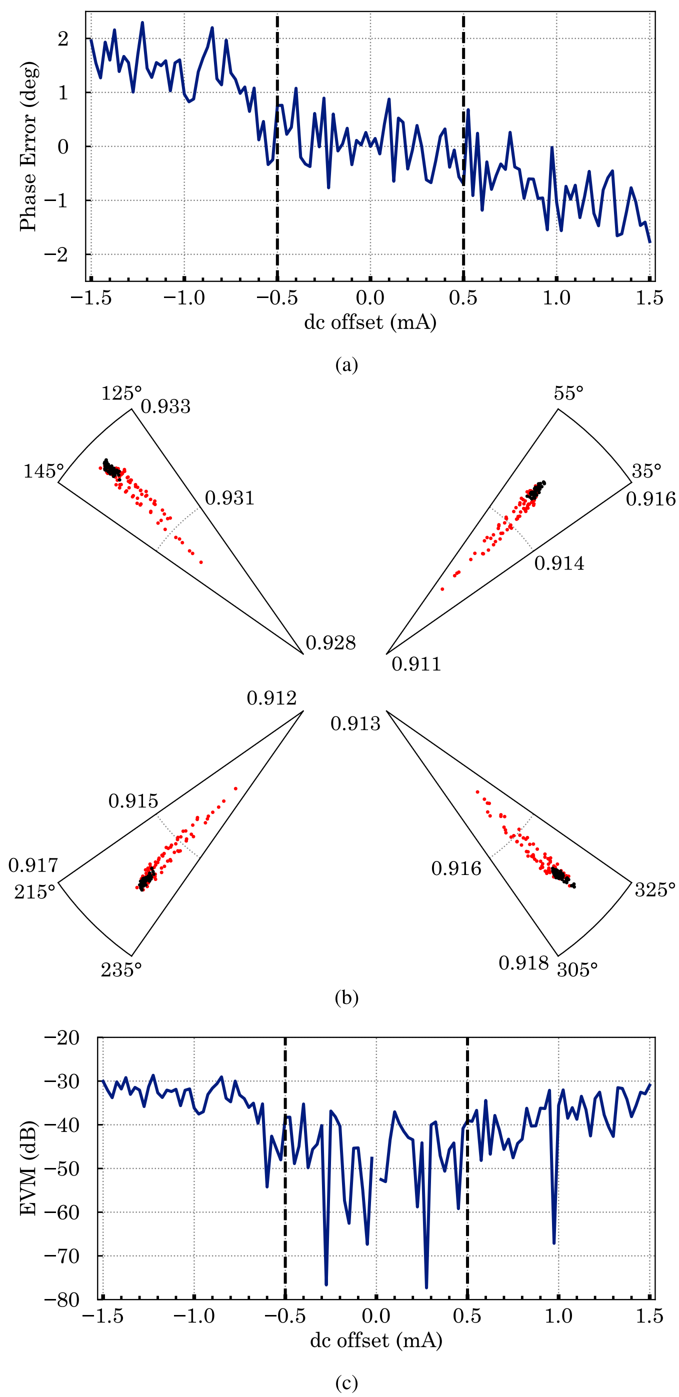

Fig. 12. (a) Residual phase error after detrending the bias-dependent phase offset in Fig. 11(c). (b) Constellation diagram of the averaged, phase detrended IQ vectors as a function of dc bias current between ±1.5 mA (points within the ±0.5-mA QLR in black and points outside the QLR in red) after downsampling to the original 10-MHz rate. (c) EVM.

multitone. The generated spectrum is shown in Fig. 10 (blue). We next perform the same dc-offset current and AWG pulse amplitude QLR measurements as with the multitone in Section III and observe the same QLR for the parameters: ±0.5-mA dc-bias QLR and from 0.310 to 335 $V_{\text{p-p}}$ or 7.8% fractional pulse-amplitude QLR. This is not surprising because both Δ–Σ patterns have similar maximum pulse densities and similar minimum spacing in time between positive and negative pulses, that is, similar total integrated power over the 40 MHz of interest. We also again measure the potential feedthrough error due to the drive current (Fig. 10, yellow) by using SW to insert a 20-dB attenuator; the error is below the noise floor of the measurement.

The measured waveforms are also analyzed in the time domain. The signal analyzer records a time trace of 400 000 IQ samples at 80 MSa/s that we split into 800-ns periods and average all of the periods (Fig. 11(a), the 95% confidence interval is equal to the line widths). Without phase detrending, changing the dc current offset creates a significant change in the time trace even within the ±0.5-mA QLR. However, we see that the amplitude error $|(t, I_{\mathrm{dc}})/IQ(t, 0)|$ (Fig. 11(b), where $IQ(t) = I(t) + j \cdot Q(t)$) is less than ±0.005 dB within the ±0.5-mA QLR (horizontal dashed lines) when symbols are generated from 200 to 600 ns. We perform a linear fit to the time-averaged phase error $\arg(IQ(t, I_{\mathrm{dc}})/IQ(t, 0))$ within the ±0.5-mA QLR (Fig. 11(c), solid-line data, dotted-line fit, and horizontal dashed QLR lines) resulting in a fit slope of −18.9°/mA with a 0.657°/mA residual standard error of the fit [34]. Using this slope to detrend the waveform timing variation within the QLR, we observe a clear QLR in terms of the time-averaged detrended phase in Fig. 12(a).

To further analyze the stability of the QPSK waveform, in Fig. 12(b), we plot the averaged, detrended data from Fig. 11 in a constellation diagram. The four symbols per time trace at each dc current are extracted by downsampling the measured 80 MSa/s IQ vectors by a factor of eight to the original 10-MHz clock rate and ignoring clock cycles without symbols. There is a tight cluster for dc current values within the ±0.5-mA QLR (black dots), but outside the QLR (red), the symbols quickly diverge from the nominal values. We quantify this divergence by calculating and plotting the error vector magnitude (EVM) $|IQ(t, I_{\mathrm{dc}}) - IQ(t, 0)|$ [35] averaged over the four-symbol period at each value of the dc current, where the IQ vectors have already been normalized. Within the dc current QLR, the EVM stays at the −48-dB average value and then diverges outside the QLR. In general, the phase noise of a signal generated by RF-JAWS is dominated by the system phase noise that is on the order of −85 dBc/Hz at a 100-Hz offset [21, Fig. 12].

V. Conclusion and Future Work

In this article, we demonstrate, for the first time, a quantum-based source of multitone and modulated waveforms. The RF-JAWS generates arbitrary waveforms with a calculable on-wafer voltage that is constant over a range of operational, bias, and environmental conditions, a requirement for ensuring the synthesized signals are quantum-based. The multitone waveform we generated using 4500 JJs with 101 tones and a flat power distribution of −53 dBm has a high SNR over 60 dB, a frequency resolution of 400 kHz, and a relatively wide bandwidth of 40 MHz. Using the same technique, we generated a QPSK waveform of quantum-based stability. The measured QLRs were similar for both synthesized waveforms, as expected for waveforms having similar total integrated power over the 40-MHz bandwidth of interest. In the future, we plan to increase the maximum output power, increase the synthesis frequency, and then perform power, cross-frequency phase, and S-parameter calibrations of our RF-JAWS system at the on-chip reference plane; this has already been done to calibrate a single-tone source [26]. In general, this work is a step toward using quantum-based sources as modulated-waveform references for communication links and microwave waveform metrology.

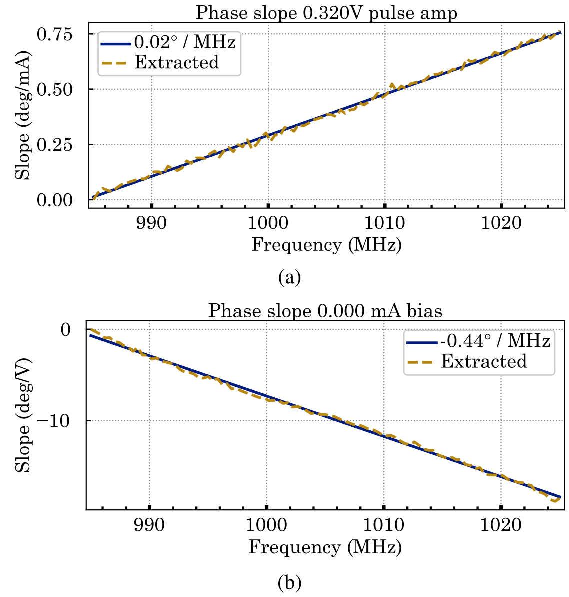

Fig. 13. (a) Slope for the dc-bias phase dependence extracted over frequency (solid) using the method explained in the Appendix, and a fit frequency-dependent slope. (b) Slope for the pulse-amplitude phase dependence extracted over frequency (solid) using the same method, and a fit frequency-dependent slope.

Appendix
Phase Detrending for Multitone QLRs

The timing dependence of the JJ-generated waveforms (and therefore of the measured phase spectrum in Fig. 4) stems from the JJ dynamics under varying drive or bias currents and was studied extensively in [27]. Prior work concludes that this timing variation is mostly linear for the type of junctions used in this work. The dependence of the measured phase spectrum on dc offset current and drive-current pulse amplitude is mathematically corrected by implementing the following algorithm.

1) For N dc-bias (pulse amplitude) sweep points, acquire complex amplitudes $A[k, j]$ ($k \in 1, 2, \ldots, 101$; $j \in 1, 2, \ldots, N$) of the 101 tones in the multitone spectra at frequencies $f[k]$ from 985 to 1025 MHz.
2) Obtain phase dependencies $\varphi[k, j]$ that are normalized by the phase at the lowest frequency

$$\varphi[k, j] = \arg \frac{A[k, j]}{e^{j \cdot \arg(A[1, j]) \cdot f[k]/f[1]}}. \tag{2}$$

3) Subtract phases at zero-bias (nominal pulse amplitude, 0.320 $\mathrm{V_{p\text{-}p}}$) at index j_0 for each frequency index k

$$\varphi'[k, j] = \varphi[k, j] - \arg A[k, j_0]. \tag{3}$$

4) Fit a slope to $\varphi'[k, j]$ over a sweeping range within the QLR using a linear regression algorithm [34] and subtract it from the entire dc-bias (pulse-amplitude) sweep to obtain the detrended $\varphi^*[k, j]$.

The resulting phase dependencies $\varphi^*[k, j]$ are essentially constant (to within the signal analyzer and trigger noise) inside the QLRs and start to vary outside the ranges, as was shown in Figs. 5–7. We plot over frequency the extracted slopes for dc-bias [Fig. 13(a)] and pulse amplitude [Fig. 13(b)] slopes in Fig. 13. Finally, we fit the resulting frequency dependencies with constant slopes to confirm the linearity of the JJ timing. The standard errors for the slope fits [34] are 0.0001°/MHz for the dc-bias dependencies and 0.0024°/MHz for the pulse-amplitude dependencies. Note that this phase detrending is effectively calibrating the dependence of the relative time delay between the current bias pulse and the resulting voltage pulse on the dc current or pulse amplitude. This calibration is expected to change if the default bias pulse shape at the JJs is changed: for example, by changing the FIR filter, the RF amplifier bias, or the signal path between the amplifier and the JJs, also partially affected by the helium level in the Dewar.

Acknowledgment

The authors would like to thank the Microfabrication Facility, National Institute of Standards and Technology (NIST), Boulder, CO, USA, for the support in the fabrication of the superconducting JAWS chips described in this work and Rob Horansky from NIST for useful discussions regarding multitone waveforms. Zoya Popović acknowledges support through the Lockheed Martin Endowed Chair in RF Engineering at the University of Colorado, Boulder. This work is a contribution of the U.S. Government and is not subject to U.S. copyright.

References

[1] N. B. Carvalho, K. A. Remley, D. Schreurs, and K. G. Gard, "Multisine signals for wireless system test and design [application notes]," *IEEE Microw. Mag.*, vol. 9, no. 3, pp. 122–138, Jun. 2008.

[2] P. D. Hale, D. F. Williams, and A. Dienstfrey, "Waveform metrology: Signal measurements in a modulated world," *Metrologia*, vol. 55, no. 5, pp. S135–S151, Aug. 2018, doi: 10.1088/1681-7575/aad1cd.

[3] J. Verspecht, "Large-signal network analysis," *IEEE Microw. Mag.*, vol. 6, no. 4, pp. 82–92, Dec. 2005.

[4] D. B. Gunyan and J. B. Scott, "Pulse generator," U.S. Patent 7 423 470B2, Sep. 9, 2008.

[5] *5989-7619EN. U9391C/F/G Comb Generators*, Technical Overview, Keysight Technol., Santa Rosa, CA, USA, Sep. 2017. [Online]. Available: http://literature.cdn.keysight.com/litweb/pdf/5989-7619EN.pdf

[6] D. F. Williams, P. D. Hale, T. S. Clement, and J. M. Morgan, "Mismatch corrections for electro-optic sampling systems," in *Proc. 56th ARFTG Conf. Dig.*, vol. 38, 2000, pp. 1–5.

[7] D. F. Williams, P. D. Hale, and T. S. Clement. (Aug. 2022). Uncertainty of the NIST Electrooptic Sampling System. Technical Note (NIST TN). National Institute of Standards and Technology. Gaithersburg, MD, USA. [Online]. Available: https://tsapps.nist.gov/publication/get_pdf.cfm?pub_id=31712

[8] A. Sanders, D. F. Williams, J. M. Kast, K. A. Remley, and R. D. Horansky, "Large-signal-network-analyzer phase calibration on an arbitrary grid," in *IEEE MTT-S Int. Microw. Symp. Dig.*, Jun. 2019, pp. 1391–1394.

[9] P. D. Hale, K. A. Remley, D. F. Williams, J. A. Jargon, and C. M. J. Wang, "A compact millimeter-wave comb generator for calibrating broadband vector receivers," in *Proc. 85th Microw. Meas. Conf. (ARFTG)*, May 2015, pp. 1–4.

[10] R. Figueiredo and N. Carvalho, "Two-tone signals harmonic conditions for PAPR variation," in *Proc. Int. Workshop Integr. Nonlinear Microw. Millimetre-Wave Circuits (INMMiC)*, Apr. 2022, pp. 1–3.

[11] K. A. Remley, P. D. Hale, D. I. Bergman, and D. Keenan, "Comparison of multisine measurements from instrumentation capable of nonlinear system characterization," in *Proc. 66th ARFTG Microw. Meas. Conf. (ARFTG)*, Dec. 2005, pp. 1–10.

[12] A. Chung, M. B. Rejeb, Y. Beltagy, A. M. Darwish, H. A. Hung, and S. Boumaiza, "High frequency and wideband modulated signal generation using frequency doublers," in *IEEE MTT-S Int. Microw. Symp. Dig.*, Jun. 2018, pp. 156–159.

[13] K. A. Remley, P. D. Hale, D. F. Williams, and C.-M. Wang, "A precision millimeter-wave modulated-signal source," in *IEEE MTT-S Int. Microw. Symp. Dig.*, Jun. 2013, pp. 1–3.

[14] R. D. Horansky, D. C. Ribeiro, J. A. Jargon, and K. A. Remley, "Dominant uncertainty in traceable millimeter-wave modulated signal source for OTA calibration," in *Proc. Int. Workshop Antenna Technol. (iWAT)*, Feb. 2020, pp. 1–4.

[15] P. Manurkar, R. D. Horansky, B. F. Jamroz, J. A. Jargon, D. F. Williams, and K. A. Remley, "Precision millimeter-wave-modulated wideband source at 92.4 GHz as a step toward an over-the-air reference," *IEEE Trans. Microw. Theory Techn.*, vol. 68, no. 7, pp. 2644–2654, Jul. 2020.

[16] J. X. Przybysz et al., "Josephson junction digital to analog converter for accurate AC waveform synthesis," U.S. Patent 5 812 078, Sep. 22, 1998.

[17] S. P. Benz and C. A. Hamilton, "A pulse-driven programmable Josephson voltage standard," *Appl. Phys. Lett.*, vol. 68, no. 22, pp. 3171–3173, May 1996, doi: 10.1063/1.115814.

[18] S. P. Benz, C. A. Hamilton, C. J. Burroughs, T. E. Harvey, L. A. Christian, and J. X. Przybysz, "Pulse-driven Josephson digital/analog converter [voltage standard]," *IEEE Trans. Appl. Supercond.*, vol. 8, no. 2, pp. 42–47, Jun. 1998.

[19] P. F. Hopkins et al., "RF waveform synthesizers with quantum-based voltage accuracy for communications metrology," *IEEE Trans. Appl. Supercond.*, vol. 29, no. 5, pp. 1–5, Aug. 2019.

[20] A. Rufenacht, N. E. Flowers-Jacobs, and S. P. Benz, "Impact of the latest generation of Josephson voltage standards in AC and DC electric metrology," *Metrologia*, vol. 55, no. 5, pp. S152–S173, Aug. 2018, doi: 10.1088/1681-7575/aad41a.

[21] C. A. Donnelly et al., "1 GHz waveform synthesis with Josephson junction arrays," *IEEE Trans. Appl. Supercond.*, vol. 30, no. 3, pp. 1–11, Apr. 2020.

[22] A. A. Babenko et al., "A microwave quantum-defined millivolt source," *IEEE Trans. Microw. Theory Techn.*, vol. 69, no. 12, pp. 5404–5416, Dec. 2021.

[23] T. V. Duzer and C. W. Turner, *Principles of Superconductive Devices and Circuits*, 2nd ed. Upper Saddle River, NJ, USA: Prentice-Hall, 1999, ch. 4.

[24] G. T. S. Pavan and R. Schreier, *Understanding Delta-Sigma Data Converters*, 2nd ed. Hoboken, NJ, USA: Wiley, 2017.

[25] N. E. Flowers-Jacobs, A. E. Fox, P. D. Dresselhaus, R. E. Schwall, and S. P. Benz, "Two-volt Josephson arbitrary waveform synthesizer using Wilkinson dividers," *IEEE Trans. Appl. Supercond.*, vol. 26, no. 6, pp. 1–7, Sep. 2016.

[26] J. A. Brevik et al., "Cryogenic calibration of the RF Josephson arbitrary waveform synthesizer," in *Proc. Conf. Precis. Electromagn. Meas. (CPEM)*, Aug. 2020, pp. 1–2.

[27] C. A. Donnelly, J. A. Brevik, P. D. Dresselhaus, P. F. Hopkins, and S. P. Benz, "Jitter sensitivity analysis of the superconducting Josephson arbitrary waveform synthesizer," *IEEE Trans. Microw. Theory Techn.*, vol. 66, no. 11, pp. 4898–4909, Nov. 2018.

[28] G. Venturini. (2015). *Python-Deltasigma*. [Online]. Available: http://www.python-deltasigma.io/

[29] M. Schroeder, "Synthesis of low-peak-factor signals and binary sequences with low autocorrelation (corresp.)," *IEEE Trans. Inf. Theory*, vol. IT-16, no. 1, pp. 85–89, Jan. 1970.

[30] B. Baek, P. D. Dresselhaus, and S. P. Benz, "Co-sputtered amorphous $Nb_x\ Si_{1-x}$ barriers for Josephson-junction circuits," *IEEE Trans. Appl. Supercond.*, vol. 16, no. 4, pp. 1966–1970, Dec. 2006.

[31] A. S. Boaventura et al., "Microwave modeling and characterization of superconductive circuits for quantum voltage standard applications at 4 K," *IEEE Trans. Appl. Supercond.*, vol. 30, no. 2, pp. 1–7, Mar. 2020.

[32] V. T. M. Sayed and A. Ferrero, *Modern RF and Microwave Measurement Techniques* (The Cambridge RF and Microwave Engineering Series). Cambridge, U.K.: Cambridge Univ. Press, 2013.

[33] S. S. Haykin and M. Moher, *Introduction to Analog and Digital Communications*, 2nd ed. Hoboken, NJ, USA: Wiley, 2007.

[34] T S Community. (2022). *Scipy.Stats.Linregress*. [Online]. Available: https://docs.scipy.org/doc/scipy/reference/generated/scipy.stats.linregress.html

[35] 3GPP. (2020). *LTE; Evolved Universal Terrestrial Radio Access (EUTRA); User Equipment (UE) Radio Transmission and Reception (3GPP TS 36.101 Version 13.2.1 Release 13)*. [Online]. Available: https://www.etsi.org/deliver/etsi ts/136100 136199/136101/13.02.01 60/ts136101v130201p.pdf

Akim A. Babenko (Graduate Student Member, IEEE) received the B.S. degree (Hons.) in electronics and nanoelectronics and the M.S. degree (Hons.) in radiophysics from Kuban State University, Krasnodar, Russia, in 2017 and 2019, respectively, with a focus on the vector network analysis of microwave mixers, and the Ph.D. degree from Prof. Popovic's Group, University of Colorado (CU) Boulder, Boulder, CO, USA, in 2022, for his work at the National Institute of Standards and Technology on the Quantum Voltage Project. He designed multidecade bandwidth passive and active MMICs in III–V and superconductor technologies and developed new measurement and signal-processing techniques for RF Josephson Arbitrary Waveform Synthesizers. Since 2022, he has been working at the Jet Propulsion Laboratory, Pasadena, CA, USA, on low-noise and quantum-limited receivers for atmospheric remote sensing and radio astronomy.

Nathan E. Flowers-Jacobs (Member, IEEE) was born in Urbana, IL, USA, on June 15, 1979. He received the B.S. degree in physics from the California Institute of Technology, Pasadena, CA, USA, in 2001, and the Ph.D. degree in physics from the University of Colorado-Boulder, Boulder, CO, USA, in 2010, for his work on a quantum-limited detector of nanomechanical motion based on electron tunneling across an atomic point contact.

He worked at the MIT Lincoln Laboratory, Lexington, MA, USA, where he was involved in modeling radar cross sections for two years before entering graduate school at JILA, Boulder. From 2010 to 2014, he was a Post-Doctoral Associate at Yale University, New Haven, CT, USA, working on nanomechanical displacement measurements at the quantum limit using optical cavities. In 2014, he joined the Quantum Voltage Project, National Institute of Standards and Technology (NIST), Boulder, where he has been working on the development, characterization, and applications of the Josephson Arbitrary Waveform Synthesizer (JAWS), an ac Josephson voltage standard based on pulse-biased arrays of Josephson junctions.

Dr. Flowers-Jacobs received the IEEE Council on Superconductivity Van Duzer Prize in 2019.

Anna E. Fox (Senior Member, IEEE) received the Ph.D. degree in electrical engineering from Drexel University, Philadelphia, PA, USA, in 2009.

From 2009 to 2010, she was a National Research Council Post-Doctoral Researcher at the Optoelectronics Division, National Institute of Standards and Technology (NIST), Boulder, CO, USA, where she worked fabricating superconducting transition-edge sensors for use at optical wavelengths. She continued her work in transition-edge sensor fabrication in the NIST Quantum Sensors Project where she fabricated arrays of Transition-Edge Sensor (TES) bolometers for cosmic microwave background detection. Since 2013, she has been with the NIST Quantum Voltage Project, pursuing the design and fabrication of voltage standard devices, such as the programmable Josephson voltage standard and the ac Josephson voltage standard.

Dr. Fox received the 2016 and 2019 IEEE Council on Superconductivity Van Duzer Prize.

Paul D. Dresselhaus was born in Arlington, MA, USA, on January 5, 1963. He received the B.S. degree in physics and electrical engineering from the Massachusetts Institute of Technology, Cambridge, MA, USA, in 1985, and the Ph.D. degree in applied physics from Yale University, New Haven, CT, USA, in 1991.

In 1999, he joined the Quantum Voltage Project, the National Institute of Standards and Technology (NIST), Boulder, CO, USA, where he has been developing novel superconducting circuits and broadband bias electronics for precision voltage waveform synthesis and programmable voltage standard systems. He has been the Project Leader of the Quantum Voltage Project, NIST, since October 2015. He was with Northrop Grumman, Linthicum Heights, MD, USA, for three years, where he designed and tested numerous gigahertz-speed superconductive circuits, including code generators and analog-to-digital converters. He also upgraded the simulation and layout capabilities at Northrop Grumman to be among the world's best. He has also been a Post-Doctoral Assistant with the State University of New York, Stony Brook, NY, USA, where he worked on the nanolithographic fabrication and study of Nb–AlO_x–Nb junctions for single-electron and Single Flux Quantum (SFQ) applications, single-electron transistors and arrays in Al–AlO_x tunnel junctions, and the properties of ultrasmall Josephson junctions.

Dr. Dresselhaus received two U.S. Department of Commerce Gold Medals for Distinguished Achievement and the IEEE Council on Superconductivity Van Duzer Prize in 2006, 2016, and 2019.

Zoya Popović (Fellow, IEEE) received the Dipl.-Ing. degree from the University of Belgrade, Belgrade, Serbia, in 1985, and the Ph.D. degree from Caltech, Pasadena, CA, USA, in 1990.

She was a Visiting Professor with the Technical University of Munich, Munich, Germany, from 2001 to 2003; ISAE, Toulouse, France, in 2014; and was a Chair of Excellence at Carlos III University, Madrid, Spain, from 2018 to 2019. She is a Distinguished Professor and the Lockheed Martin Endowed Chair in electrical engineering at the University of Colorado, Boulder, CO, USA. She has graduated over 70 PhDs and currently advises 18 doctoral students. Her research interests are in high-efficiency power amplifiers and transmitters, microwave and millimeter-wave high-performance circuits for communications and radar, medical applications of microwaves, quantum sensing and metrology, and wireless powering.

Dr. Popović was elected as a Foreign Member of the Serbian Academy of Sciences and Arts in 2006. She was elected as a member of the National Academy of Engineering in 2022. She was named the IEEE MTT Distinguished Educator in 2013 and the University of Colorado Distinguished Research Lecturer in 2015. She was a recipient of two IEEE MTT Microwave Prizes for best journal articles, the White House NSF Presidential Faculty Fellow Award, the URSI Issac Koga Gold Medal, the ASEE/HP Terman Medal, and the German Alexander von Humboldt Research Award.

Samuel P. Benz (Fellow, IEEE) was born in Dubuque, IA, USA, on December 4, 1962. He received the B.A. degree (summa cum laude) in physics and math from Luther College, Decorah, IA, USA, in 1985, and the M.A. and Ph.D. degrees in physics from Harvard University, Cambridge, MA, USA, in 1987 and 1990, respectively.

In 1990, he joined the National Institute of Standards and Technology (NIST), Boulder, CO, USA, as a NIST/NRC Post-Doctoral Fellow and became a permanent Staff Member in January 1992. He has been the Project Leader of the Quantum Voltage Project, NIST, since October 1999, and the Group Leader of the Superconductive Electronics Group since 2015. He has worked on a broad range of topics within the field of superconducting electronics, including Josephson junction array oscillators, single flux quantum logic, ac and dc Josephson voltage standards, Josephson waveform synthesis, and noise thermometry. He has over 290 publications and is the holder of four patents in the field of superconducting electronics.

Dr. Benz is a Fellow of NIST and the American Physical Society (APS). He is a member of Phi Beta Kappa and Sigma Pi Sigma. He was received the R. J. McElroy Fellowship from 1985 to 1988 for his Ph.D. degree, three U.S. Department of Commerce Gold Medals for Distinguished Achievement, the 2016 IEEE Joseph F. Keithley Award, and the IEEE Council on Superconductivity Van Duzer Prize in 2006, 2016, and 2019.